



Agir, M. B., White, C. and Kontis, K. (2022) Impact of stagnation temperature and nozzle configuration on rarefied jet plume interactions. *Journal of Spacecraft and Rockets*, 59(5), pp. 1536-1551. (doi: [10.2514/1.A35362](https://doi.org/10.2514/1.A35362))

There may be differences between this version and the published version. You are advised to consult the published version if you wish to cite from it.

<http://eprints.gla.ac.uk/268663/>

Deposited on 6 April 2022

Enlighten – Research publications by members of the University of Glasgow  
<http://eprints.gla.ac.uk>

# Impact of Stagnation Temperature and Nozzle Configuration on Rarefied Jet Plume Interactions

Muhammed Burak Agir <sup>\*</sup>, Craig White <sup>†</sup> and Konstantinos Kontis <sup>‡</sup>  
*James Watt School of Engineering, University of Glasgow, Glasgow, UK, G12 8QQ.*

The canting axis of thrusters on space platforms, which likely operate in a vacuum environment with a high degree of flow rarefaction, is significant in order to create the desired torque for manoeuvring, maintaining orbit, eliminating perturbation forces, docking, etc. Therefore, the interactions of expanding plumes with one another and with solid surfaces in multi-nozzle arrays are inevitable. In order to gain a better understanding of the effect of nozzle configurations and conditions on the plume-plume and plume-surface interactions, a simulation matrix is carried out for a sonic nozzle using the direct simulation Monte Carlo method with the *dsmc-Foam+* code. As nozzle arrays are packed more tightly together, the plume-plume interactions become stronger, which has an influence on the stagnation line density and temperature profiles. For a given stagnation temperature, the spacing between nozzles in the array does not have a strong influence on the normalised surface pressure, but there is an increase in the maximum normalised shear stress as the distance between the nozzles increases. There is a significant difference in the results for double and quadruple nozzle arrays, with greater normalised stagnation pressures and shear stresses found as the number of nozzles in the array is increased. For a single nozzle, increasing the stagnation temperature does not have a significant effect on the normalised surface pressures, but does increase the maximum normalised shear stress and increases the measured heat flux on the surface. For arrays of double and quadruple nozzles, the number of nozzles has a much greater influence on the measured surface properties than the stagnation temperature.

## Nomenclature

$A_{pl}$	=	plume constant, [-]
$\mathbf{c}$	=	velocity vector of a molecule, [-]
$D$	=	centre-to-centre distance between nozzles, [mm]
$F$	=	force, [N]

---

<sup>\*</sup>Ph.D. Student, Member of AIAA

<sup>†</sup>Lecturer in Aerospace Sciences

<sup>‡</sup>Mechan Chair of Engineering/Professor of Aerospace Engineering, FAIAA.

<b>F</b>	=	external force, [N]
<i>f</i>	=	velocity distribution function, [-]
<i>H</i>	=	hovering altitude, [mm]
<i>I<sub>sp</sub></i>	=	specific impulse, [N · s/kg]
<i>Kn</i>	=	Knudsen number, [-]
<i>k</i>	=	gas thermal conductivity, [W/m · K]
<i>L</i>	=	characteristic length, [m]
<i>l</i>	=	half axial distance of the flat impingement plate, [mm]
<i>Ma</i>	=	Mach number, [-]
<i>m</i>	=	molecular mass, [kg]
<i>n</i>	=	number density, [-]
<i>nf</i>	=	product of number density, [-]
<i>P</i>	=	pressure, [Pa]
<i>q</i>	=	heat flux, [W/m <sup>2</sup> ]
<i>R</i>	=	gas constant, [J/K · mol]
<i>Re</i>	=	Reynolds number, [-]
<i>r</i>	=	cross-sectional radius of a nozzle exit, [mm]
<b>r</b>	=	position vector of a molecule, [-]
<i>T</i>	=	temperature, [K]
<i>t</i>	=	time, [s]
<i>u</i>	=	flow velocity, [m/s]
<i>V</i>	=	velocity, [m/s]
<i>x</i>	=	a distance from the reference point on the surface, [m]
<i>Z</i>	=	collision numbers, [-]
<i>z</i>	=	radial distance, [m]

#### Greek Letters

$\alpha$	=	angle of attack, [°]
$\beta$	=	impingement angle, [°]
$\Gamma$	=	characteristic temperature, [K]
$\gamma$	=	specific gas constant, 1.4
$\zeta$	=	effective degrees of freedom, [-]
$\Theta$	=	polar angle, [°]

$\kappa$	=	hypersonic parameter, [-]
$\Lambda$	=	recovery factor, [-]
$\lambda$	=	mean free path, [m]
$\mu$	=	dynamic viscosity, [kg/m · s]
$\phi$	=	thermal accommodation coefficient, [-]
$\rho$	=	density, [kg/m <sup>3</sup> ]
$\sigma$	=	collision cross-section, [m <sup>2</sup> ]
$\tau$	=	shear stress, [N/m <sup>2</sup> ]
$\Omega$	=	solid angle, [°]
$\omega$	=	viscosity exponent, 0.74

#### Subscripts

<i>a</i>	=	ambient
<i>c</i>	=	Chapman-Enskog coefficient
<i>d</i>	=	design
<i>dyn</i>	=	dynamic
<i>int</i>	=	internal
<i>lim</i>	=	limit
<i>mc</i>	=	mean collision
<i>mp</i>	=	most probable thermal
<i>n</i>	=	nozzle throat
<i>ov</i>	=	overall
<i>p</i>	=	penetration
<i>pl</i>	=	plume
<i>prop</i>	=	propellant
<i>r</i>	=	relative
<i>ref</i>	=	reference
<i>res</i>	=	cell residence
<i>rot</i>	=	rotational
<i>s</i>	=	on the flow streamline
<i>sonic</i>	=	at sonic velocity
<i>st</i>	=	static
<i>T</i>	=	thrust

$t$	=	total
$tr$	=	translational
$w$	=	wall
$x$	=	in the x-axis
$y$	=	in the y-axis
0	=	stagnation
1	=	parameters of molecule-1

#### Superscripts

*	=	post-collision variables
^	=	normalised
-	=	average
·	=	flux

## I. Introduction

ASSORTED types of thrusters with different propellants and sizes are employed for space missions of launching, attitude control, maintaining orbit, manoeuvring, etc. These platforms have a wide thrust range from 1 mN to millions of Newtons. Depending on the possible perturbation forces and targeted accuracy of a platform's position, the location of rockets on the platform and their thrust may vary to reach the desired torque requirements.

The pressurised exhaust gas is expanded through a nozzle geometry and exits to the surrounding atmosphere and forms a plume. Rocket exhaust plumes have different properties depending on mass flow rate, stagnation pressure and temperature, environmental conditions in which exhaust gases are released, and the type of propellant used. Additionally, before the exhaust products enter into the nozzle, the flow is heated in some cases to gain maximum efficiency and to increase the specific impulse. For these reasons, the exhaust gas temperature alters due to the propellant types or thrust demands. In addition, the plume forms depending on the altitude as the ambient pressure decreases and the plume transitions from under expanded to over expanded.

Furthermore, the mission type or operation of space platforms has an impact on the plume impingement on a solid surface. Mass flux of exhaust gas products impinging on a surface may be greater during docking operations than in orbit control manoeuvres since it is assumed that the relatively dense portion of the plume interacts with the surface during docking [1].

Depending on the nozzle location, plume-surface interactions can form compressed shocks and boundary layers, which can be obtained in continuum flow. However, in a vacuum environment, the shape of plumes changes such that a barrel shock no longer exists, plumes tend to expand further, etc. Dettleff [1] explains the expansion of low-density

exhaust plumes in vacuum environments with higher velocities as "[t]he nozzle area ratio [...] is typically in the order of 50 so that the exit Mach number is 5". Therefore, highly expanded and accelerated plumes tend to interact more with other plumes in multi-nozzle systems and the surfaces of platforms through diffusion and scattering in space applications. Plume flow problems have been investigated by Vick *et al* [2], Boettcher and Legge [3], Lengrand [4], etc. as stated in Ref. [1] and for various impingement scenarios, such as perpendicular impingement to the surface [5], laterally located thrusters on the sides of platform bodies [6, 7], and for nozzles positioned at an angle to the surface [8–10]. These studies contribute a better understanding for some problems in application. This is a significant research interest since impingement affects operational lifetime and essential functions of platforms.

The impingement effect of the different types of plumes, such as cold gas, chemical reaction productions, and ion thrusters, on a spacecraft surface – in terms of the ejecta dynamics and plume physics as mentioned in Ref. [11] – has been a significant topic of both numerical and experimental studies for some time. Thus, the modelling of single plume and multi-plume interactions at different ambient conditions are the first step of the impingement examinations. A single exhaust plume may start in the continuum regime and tend towards the free-molecular regime as it expands, and so the employed numerical approach for plume modelling may differ or hybrid approaches may be required for a complete solution.

Ivanov and Markelov [12] simulated spacecraft which operate in low Earth orbit. These platforms create their own ambient atmosphere (OAA) due to the use of Reaction Control Systems (RCS) that are formed of multiple thrusters. Therefore, the peripheral effect of OAA was a research interest for the Astra-2 experiment, where the plume of a cold argon thruster interacted with the Mir Space Station (MSS). This computational study presents a wide-range of solutions for the various flow regimes of the plume, from continuum to rarefied, in a large spatial scale from the nozzle to the far-field. The simulation of the plume was conducted the using Navier-Stokes (NS) equations for the continuum part, direct simulation Monte Carlo (DSMC) for the rarefied part, and the test particle Monte Carlo (TPMC) for the free-molecular regime section of the plume. In another study by Ivanov *et al* [13] presents the same complete solution approach for a different plume simulation. The interaction between two parallel nitrogen free jet plumes was modelled with a 3D DSMC code to investigate the plume-plume interactions. For the plume-surface interactions, the simulation of a plume exhausted by a 20 N thruster impinging on the surface of the European Space Agency (ESA)'s XMM satellite was conducted by employing the TPMC method. The results of the impingement simulations of two plumes indicate that a total axial force of 6.2 N, which corresponds to the loss of 15% of the total nominal thrust of the two thrusters, is created on the surface. Another computational fluid dynamics (CFD)-DSMC modelling [14] approach was conducted for the plume-surface interactions by NASA to simulate the docking case, named F3U, of an orbiter to the MSS during the STS-74 mission. However, these studies do not present detailed solutions for the effect of multi-nozzle configurations and changing stagnation temperatures on the plume-plume and plume-surface impingement parameters in a vacuum environment.

A further study on a CFD-DSMC combined approach [15] is employed to model the plume of a monopropellant thruster while discharging a jet flow plume into a vacuum environment. A NS solver is applied to predict the flow physics around the nozzle exit, and DSMC provides a solution to the far-field for the three types of propellant species of  $H_2$ ,  $N_2$ , and  $NH_3$ . A complete analysis of nozzle plume systems is also proposed by Ref. [16] through dividing the control volume of interest into two parts as CFD and DSMC regions, with coupling at the continuum breakdown location.

Different coupled methods have been also applied to simulate the plume in further studies. Boyd and Starkt [17] simulated the combustion processes and produced the data for the expanded plume from various radial distances by employing the Simons model [18], the Method of Characteristic (MOC) [19], and DSMC. Although the motivation of plume-spacecraft surface interaction initiated this study, the work solely focuses on the change in the flow parameters from the inside of the thruster to the far-field of the plume. The plume of a monopropellant hydrazine thruster is simulated using DSMC and MOC in Ref. [20] and the authors state that DSMC offers more accurate data than MOC for the estimation of surface impingement effects at the free molecular regime of the plume. For the modelling of flows in rocket nozzles and rarefied exhaust plumes, various approaches have also been implemented in the solution frame of DSMC. An optimised hybrid model of Fokker-Planck (FP) and DSMC aims to provide a lower computational cost by applying the FP method and a higher accuracy from DSMC only where required [21]. The use of DSMC is also extended for the modelling of flow in micro/nanoscale converging-diverging nozzles with the application of unstructured meshes [22] and the simplified Bernoulli trial (SBT) method [23].

For the plume-plume interactions, an investigation of four JP4/LOX 500 lbf water-cooled rocket engines at two different ambient pressures was experimentally and numerically conducted to measure the plume-induced base pressure and heating parameters. The simulation of the plume physics was completed using the Loci-CHEM NS CFD solver for the highest-fidelity predictions [24]. The study shows the importance of plume-plume interaction research, but falls short in covering a solution for the plumes at rarefied regimes. Another study [25] describes a methodology to solve the plume-plume and plume-surface interaction for single and double nozzle(s) applications during the docking maneuver of a shuttle orbiter to the MSS. Three regimes of plume flow-field are simulated using the NS equations and DSMC; the impingement of the plume with the surface is also simulated with DSMC. The pressure forces on the surface of the MSS and the changes in plume density are calculated for different nozzle types, such as single and double with various thruster types. Further outcomes of the plume, including velocity, temperature, surface shear stress, surface heating, etc. and the changes in configuration of the nozzles at the dual systems are not provided.

Boyd *et al* [26] performed DSMC simulations for expanding nitrogen flow into a near-vacuum condition through a small sonic nozzle, and also compare the results to experimental data. Afterwards, another DSMC simulation was conducted by Boyd *et al* [5] to provide a solution for another plume impingement problem during a space-based experiment. The authors conducted a series of numerical simulations to further understand the effect of the impingement

angle of the plume, and the plume quantities with changing mass flow rate such as dynamic pressure and mass flux. In this study, there was no mention of the computational DSMC code, plume-plume impingement, the effect of altering stagnation temperature, and the impingement surface parameters.

Kannenbergh [8] investigated several types of problems, such as a nitrogen plume impinging on an axisymmetric body, the plume effect of a hydrazine thruster on a solar array panel, the impact of a free nitrogen jet onto an inclined flat surface, etc. using the DSMC method. The flat plate impingement case in this work is based on experiments conducted in DLR's high vacuum facility in Göttingen to measure the pressure and shear stress [9] and heat transfer [10] on a flat plate beneath the nozzle. In order to assess numerically the effect of the orientation of the impingement surface, a geometrical setup of the single plume simulations was performed, ranging the angle of attack from 90 to 0 degrees. The DSMC method indicated promising results in the validation cases when compared with the experiments. The flat plate impingement cases in this study provides the changes in plume and surface parameters as a function of the plume impingement angle from a single thruster.

The present study aims to improve the understanding of the plume-plume and plume-surface interactions in a vacuum environment. Firstly, the distance between the nozzles in a double and quadruple thruster set up is altered to examine the effect on plume-plume and plume-surface properties. In addition to the investigation of the geometrical effects, the changes in plume structure and impingement on the surface with heated flow is evaluated by increasing the stagnation temperature of the plume jet flow. Thus, this study presents a wide simulation matrix with varying nozzle-to-nozzle distance for multi-nozzle applications, and a range of stagnation temperatures for single and multi-thruster systems. Two-dimensional (2D) axisymmetric and three-dimensional (3D) DSMC simulations are carried out by using *dsmcFoam+* code.

## II. Methodology

### A. Numerical Technique

Operation in a high vacuum environment induces flow in the rarefied regime, where local thermodynamic equilibrium assumptions break down. With this, the Navier-Stokes-Fourier (NSF) equations become questionable as the linear transport and constitutive relations such as heat transfer and shear stress become inapplicable, i.e.  $q \neq k(dT/dx)$  and  $\tau \neq \mu(du/dy)$ . The dimensionless Knudsen number dictates the degree of rarefaction, which is  $Kn = \lambda/L$ , where  $\lambda$  is the mean free path, in other words, the average distance that a gas atom/molecule travels between successive inter-molecular collisions. Meanwhile,  $L$  is the characteristic length of the problem. When  $Kn > 0.001$ , the frequency of gas-surface interactions reduces and non-equilibrium effects near surfaces become significant. With further increase in Knudsen number, the flow behaviour approaches the transition regime, where  $10 > Kn > 0.1$ . Herein, although inter-molecular collisions take place, the rate of collisions are not sufficient to maintain local thermodynamic equilibrium



of the bulk flow. With reaching  $Kn < 10$ , the inter-molecular collisions do not present a significant mechanism for the transfer of mass, momentum, and energy. Thus, the collisionless Boltzmann equation can be employed to accurately predict the flow phenomena and correct flow physics.

In order to define all rarefaction regimes, the Boltzmann equation, which is an integro-differential expression, was offered by Boltzmann and is shown in Eq. 1 for a single species monatomic gas. This equation can be used for dilute gases and for all ranges of Knudsen number. Therefore, the Boltzmann equation is used to derive the physical concepts and assumptions of dilute gases by computational approaches. Garcia [27] states that there are also many computational methods that use stochastic approaches, which have been developed, and direct simulation Monte Carlo (DSMC) is one such dominant method. The DSMC method was pioneered by Bird [28] to provide a probabilistic solution to rarefied gas problems.

$$\frac{\partial}{\partial t}(nf) + \mathbf{c} \frac{\partial}{\partial \mathbf{r}}(nf) + \mathbf{F} \frac{\partial}{\partial \mathbf{c}}(nf) = \int_{-\infty}^{\infty} \int_0^{4\pi} n^2 (f^* f_1^* - f f_1) c_r \sigma d\Omega d\mathbf{c}_1 \quad (1)$$

The Boltzmann is a numerically expensive equation to solve, however, DSMC provides a solution by applying a stochastic particle-based approach, which employs *representative simulators* in phase space [29–32] to replicate real gas atoms/molecules. With this particle packing method, a DSMC simulator represents a large number of real particles to decrease computational expense. In order to record accurate statistic, Hadjiconstantinou *et al* [33] states that at least 20 simulators should be populated in each DSMC cell.

The first step of the DSMC loop starts with the movement of the particles ballistically due to their current velocity vectors and the time-step. The interaction of particles with boundaries is calculated during this phase. The Maxwellian number flux is employed to generate new DSMC particles across boundary interface, with an equilibrium distribution usually assumed. Following this, the indexes of particles due to their cell locations are registered to prepare the particles for the inter-molecular collision phase. Herein, collisions are handled stochastically while the velocity of the particles are reset and the energy exchange takes place between various modes (translational, rotational, vibrational, rotational, electronic). Several methods [32, 34–39] can be employed to ensure the correct number of inter-molecular collisions take place. In this study, the inter-molecular collision rate is controlled by the no-time-counter (NTC) scheme.

In order to represent the real gas molecules with the effects of diffusivity and viscosity of particles, Bird [40] presented a model called variable cross-section hard sphere (VHS). This model recovers the viscosity of the gas and the mean free path, providing good agreement with empirical results. Furthermore, VHS combines the simplicity of the hard sphere model with the accuracy of the inverse power law of viscosity.

DSMC simulations, which are unconditionally transient, must be run until they reach a pseudo-steady condition. The sampling of the particle properties can then be collected for a long enough run to decrease the scatter in the macroscopic fields [33]. It should be emphasised that the scatter is not due to the nature of the stochastic method and is in fact a

physical phenomena that is present in fully deterministic methods such as molecular dynamics.

## B. Computing Code

*dsmcFoam+* is a DSMC solver, developed for dilute gas problems within OpenFOAM (**Open**-source **F**ield **O**peration **A**nd **M**anipulation) version 2.4.0 [41–43]. Steady and transient DSMC simulations can be modelled various models including VHS and NTC [41]. The algorithm of *dsmcFoam+* is:

- 1) create a control volume and division into DSMC cells;
- 2) determining the boundary and initial conditions;
- 3) DSMC particle initialisation;
- 4) movement of DSMC particles;
- 5) collision calculations;
- 6) sampling of DSMC particle properties.

In order to promote the collisions of the nearest-neighbour particles, virtual *sub-cells*, which are a fraction of a DSMC cell, are created. In part 3, while populating the mesh with with DSMC particles, the user-defined macroscopic properties are used. Additionally, a loop in the algorithm repeats steps 4-6 each time-step and the simulation stops once it reaches the end-time. If the DSMC simulation is not transient, the simulation is run until the steady-state condition is reached, after which a further run is needed to decrease the scatter in the measured macroscopic values.

## III. Problem Description

The combustion temperature of rocket propellants can change depending on the propellant type and burn time. In a vacuum environment, a highly under-expanded exhaust flow will create a wide plume with a high Mach number due to free expansion downstream [1]. As such, highly rarefied expanding plumes can interact with both the surfaces of space platforms that thrusters are mounted on, and each other in a system that consists of multi-nozzles.

In this study, rarefied free jets of nitrogen and impingement on a flat plate are investigated using the DSMC method. These are performed for single and multi-nozzle configurations. The numerical works are performed by *dsmcFoam+*. Initially, a single plume, generated by a sonic orifice, with a stagnation temperature  $T_0$  of 300 K is performed, due to the availability of numerical and experimental studies [8–10] for benchmarking. Afterwards,  $T_0$  is gradually increased up to 1000 K while maintaining the 1000 Pa stagnation pressure. At a sonic speed, the ratio of total pressure to stagnation pressure,  $P/P_0$ , and the ratio of total temperature to stagnation temperature,  $T/T_0$  are calculated as 0.528 and 0.833, respectively. The Knudsen number also changes with the stagnation temperature through the relation,

$$Kn = \frac{Ma}{Re} \sqrt{\frac{\gamma\pi}{2}}. \quad (2)$$

As an example, the initial flow properties of rarefied exhaust gas in the axisymmetric domain with varying stagnation temperatures are summarised in Table 1.

**Table 1 Initial properties at the sonic nozzle exit for the different stagnation temperatures for axisymmetric single plume applications.**

$T_0$ (K)	$Kn$	$Re$	$n$ ( $m^{-3}$ )	$V_{sonic}$ (m/s)
300	0.008	147.9	$1.53 \times 10^{-23}$	322.3
400	0.011	103.5	$1.14 \times 10^{-23}$	372.1
500	0.015	78.5	$9.19 \times 10^{-22}$	416.1
600	0.019	62.6	$7.66 \times 10^{-22}$	455.8
700	0.023	51.7	$6.56 \times 10^{-22}$	492.3
800	0.028	43.8	$5.74 \times 10^{-22}$	526.3
900	0.032	37.8	$5.10 \times 10^{-22}$	558.2
1000	0.037	33.2	$4.59 \times 10^{-22}$	588.4

The VHS model is employed to simulate the collisions and the energy exchange between modes is handled with a serial application of the Larsen-Borgnakke technique. The VHS model properties of nitrogen are presented in Table 2.

**Table 2 VHS parameters of nitrogen exhaust gas.**

$\omega$	0.74
$d_{ref}$	$4.07 \times 10^{-10}$
$m$	$46.5 \times 10^{-27}$
$Z_{rot}$	5

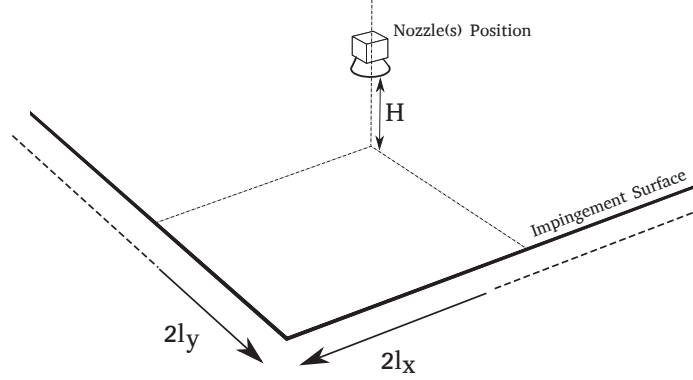
The interactions of multiple plumes with each other and the impingement of single and multiple plumes on a flat surface are investigated using an illustrated numerical setup, referenced from a numerical study [8]. A circular sonic nozzle, with an exit radius of 1 mm is located at  $H = 40$  mm above a flat plate, which is modelled as a fully diffuse Maxwellian wall held at a fixed temperature of 300 K. The surface is large enough,  $2l_x = 240$  mm  $\times$   $2l_y = 240$  mm in size in order to be able to observe the impingement effects such as surface friction coefficient, temperature and pressure distribution, etc. and to analyse backflow reflected from the plate. The problem geometry is shown in Figure 1.

The DSMC cell size and time-step should be smaller than mean free path and mean collision time, respectively, in order to obtain an accurate solution. The mean free path can be calculated using the VHS model as,

$$\lambda = (2\mu_c/15)(7 - 2\omega)(5 - 2\omega)(2\pi RT)^{-1/2}/\rho \quad [40]. \quad (3)$$

Using Eq. 3, the mean free path is calculated as  $8.269 \times 10^{-6}$  m at the stagnation temperature of 300 K. Other DSMC variables are needed to determine the selection of the time-step, such as the most probable thermal velocity  $V_{mp}$ , the mean collision time  $t_{mc}$ , and the cell residence time  $t_{res}$ . These have been calculated and are presented in Table 3.

The time-step and cell size are chosen as  $5 \times 10^{-9}$  s and  $3 \times 10^{-6}$  m according to the calculations, respectively.



**Fig. 1 Schematic of flate plate impingement.**

**Table 3 Microscopic values for free-jet flow at  $T_0 = 300$  K for axisymmetric single plume applications.**


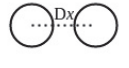
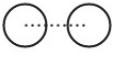
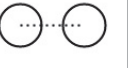
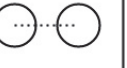

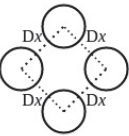
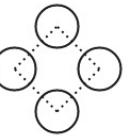
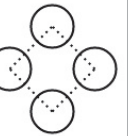
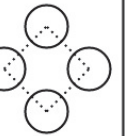






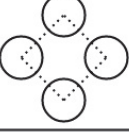
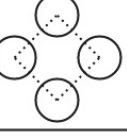
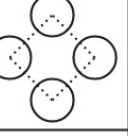
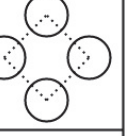


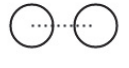
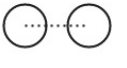
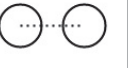
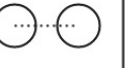
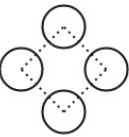
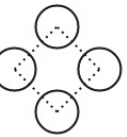
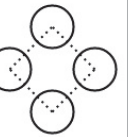
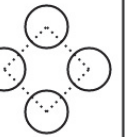







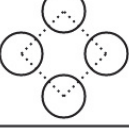
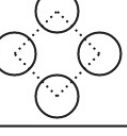
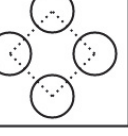
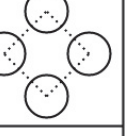



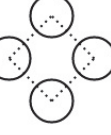
$V_{mp}$ (m/s)	85.227
$t_{res}$ (s)	$1.13 \times 10^{-8}$
$t_{mc}$ (s)	$2.15 \times 10^{-8}$

### A. Axisymmetric mesh simulations

In order to reduce the computational demand, the benchmarking simulation, with the 300 K stagnation temperature, is completed in a 2D axisymmetric domain; a half-symmetry simulation is also performed to validate the results for the 3D applications. The radial weighting factor (RWF) method is employed in the axisymmetric simulations to balance the number of particles between the cells around the axis of rotation and distant cells [44]. In a typical axisymmetric dsmcFoam+ simulation, the *nEquivalentParticles* parameter is set so that there are a sufficient number of DSMC particles in the cells near the radial origin where the radial weighting factor is close to unity, and the the maximum radial weighting factor is used to keep the number of DSMC particles to a manageable level as the cell volumes increase with radial distance. The expansion ratio of the cells are increased radially and axially since the local mean free path increases and larger mesh sizes are sufficient to capture the collisions. A mesh with a total of 440,380 cells is used. The DSMC particles are introduced at the inlet patch corresponding to the sonic nozzle exit plane and move through the control volume as the simulation proceeds.

### B. Quarter-symmetry mesh simulations

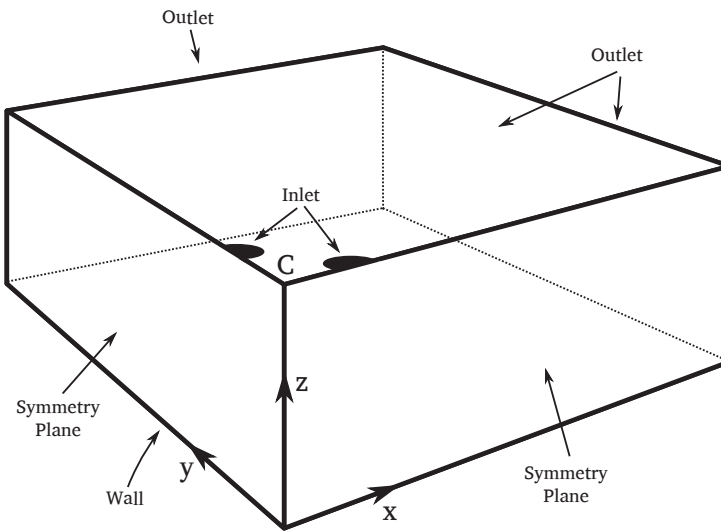
Promising results are achieved using an axisymmetric mesh when compared with Ref. [8–10]. There is no question of whether the multi-nozzle simulations can use an axisymmetric mesh topology. In order to increase the number of nozzles and verify the use of quarter and half symmetrical simulations, the problem at  $T_0 = 300$  K is repeated using

$T_0$	Single Plume	D3	D6	D9	D12
300 K					
					
400 K					
500 K					
					
600 K					
700 K					
					
800 K					
900 K					
1000 K					
					
 Axisymmetric Mesh		 Double Nozzle Configuration			
 Half-symmetric Mesh		 Quadruple Nozzle Configuration			
* The parameter x of Dx represents the distance between nozzle centres in mm.					

**Fig. 2 The matrix of rocket plume-surface simulations according to mesh topology and nozzle configurations.**

a half symmetry mesh topology and the outcomes of both simulations overlap. After verification and benchmarking simulations, a matrix of simulations is designed as given in Figure 2 to investigate both the plume-plume interactions and the changes in the surface properties depending on number of plumes and stagnation temperature.

Multi-nozzle simulations are run in the same dimensions as used for the axisymmetric mesh. A control volume is created by 3D hexahedral blocks and the patches are specified as outlet, symmetry plane, and wall, as shown in Figure 3. Creating a half-circular inlet and mirroring the geometry/entire control volume at the symmetry planes significantly reduces the computational cost of the quarter-symmetry simulation run. The corner point ‘C’ – the mid-point of the distance  $x$  given in Figure 2 – marks the half distance ( $x/2$ ) between the two inlet patches, the first of which is placed in the control volume and the second, virtually mirrored by the symmetry plane. The wall patch with a surface temperature of 300 K represents the flat plate.



**Fig. 3** The mesh topology of quadruple plume simulation.

#### IV. Results and Discussion

The accuracy of the *dsmcFoam+* simulations at  $T_0 = 300$  K is verified against numerical [8] and experimental data [9, 10]. Although the properties and measurements of the plume flow field are not provided by the experiments, the prediction of surface parameters by the numerical methods indicate accurate results, therefore, it can be deduced that the flow is captured correctly. In order to compare the prediction of DSMC solvers with the experiments [9, 10], surface parameters are plotted. The surface shear stress and pressure are normalised as,

$$\hat{\tau} = \frac{\tau}{p_0} \left( \frac{H}{r} \right)^2, \quad (4)$$

and

$$\hat{p} = \frac{p}{p_0} \left( \frac{H}{r} \right)^2, \quad (5)$$

respectively, where  $p_0$  is maintained at 1000 Pa for all cases.

As Kannenberg [8] states, the flow is free molecular at the surface. The change in density and mean free path are assumed to vary with the square of the distance from the nozzle exit. Therefore, the Knudsen number at the surface reaches the order of 10. The surface parameters in the free molecular regime depend on the properties of the incoming flow to the surface as the scattering particles do not interact with the incoming gas and the surface. In Ref. [8], the pressure on a point is expressed as the integration of normal momentum flux over the scattering and incoming particles [45] and the density is modelled depending on the throat density and the location in a polar coordinate system [46]. The other surface parameters, such as surface shear stress, transferred energy, etc. can be derived from tangential momentum and the energy difference of the integral of scattering and incoming particles as previously applied for the surface pressure and density. In order to eliminate the effects of dependence to the variables in the calculations, the normalisation is applied, however, the effect of stagnation pressure cannot be neglected as shown in Eqs (4) and (5).

#### A. *dsmcFoam+* benchmarking simulations of single plume application

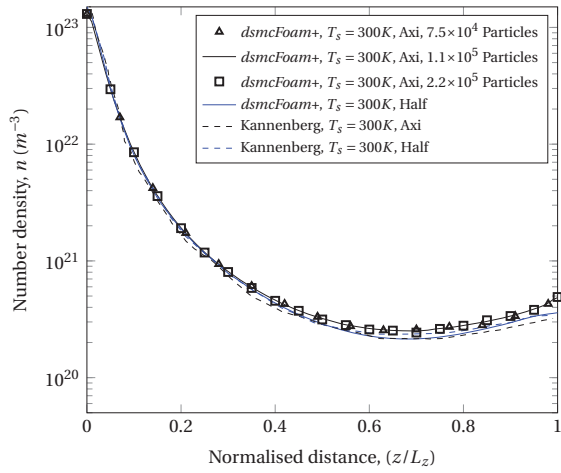
In this case, the consistency of *dsmcFoam+* results with the mesh topologies of axisymmetric and half-symmetry are compared with Refs. [8], [9], and [10] for the normal impingement of an exhaust plume on the surface at  $T_0$  of 300 K. The simulations are carried out with  $7.5 \times 10^4$ ,  $1.1 \times 10^5$ , and  $2.2 \times 10^5$  DSMC particles for the axisymmetric mesh, and  $17.2 \times 10^6$  for half-symmetric mesh. The axisymmetric mesh solutions are run until the time of 0.005 s, and the half-symmetric simulation is kept running until 0.00125 s. The sampling procedure is started as soon as possible once the simulations become steady-state. The results are shown as a function of distance,

- *line 1*: through an axial line extending from the centre of the nozzle exit to the surface, and
- *line 2*: through a radial line, which is from a point directly below the exit of the nozzle to the end point of the surface for the surface measurement.

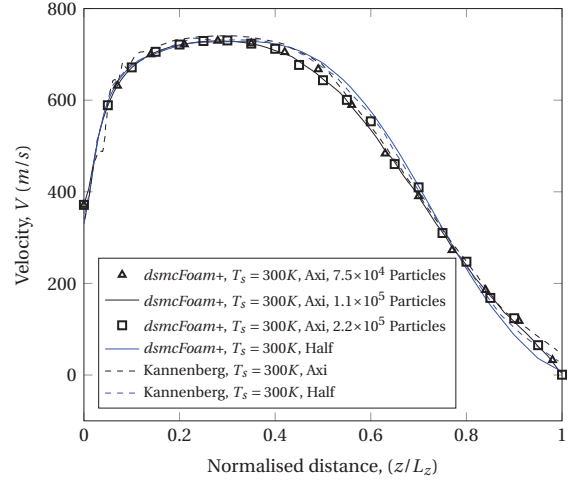
The normalised results show good agreement with the referenced data sets and the patterns show the same trend. The benchmarking dataset of plume and surface parameters are compared in Figure 4. The axisymmetric results indicate that the smallest number of particles returns results that are in agreement with the same simulations utilising more particles.

##### 1. Plume parameters

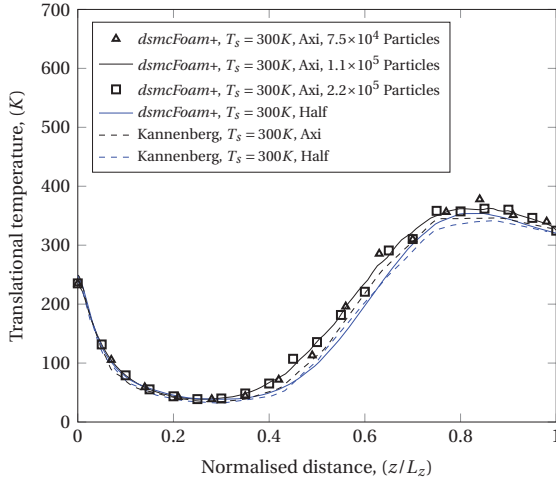
Complementing the experimental data, the simulation results show how the plume parameters change along an axial line directly below the nozzle exit, see Figures 4(a-c). It is clear that the flow density initially decreases proportionally



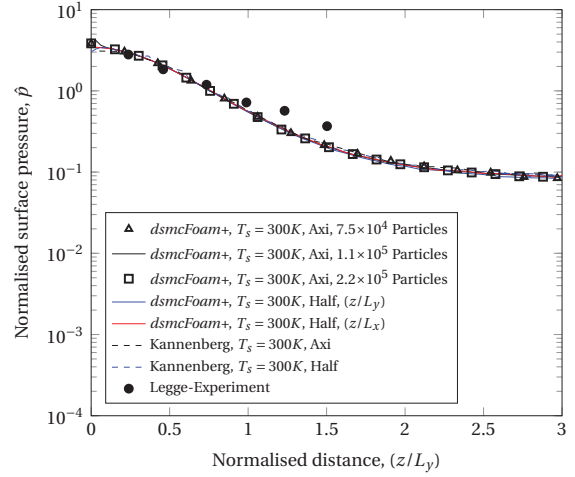
(a) Number density from the nozzle outlet to the surface.



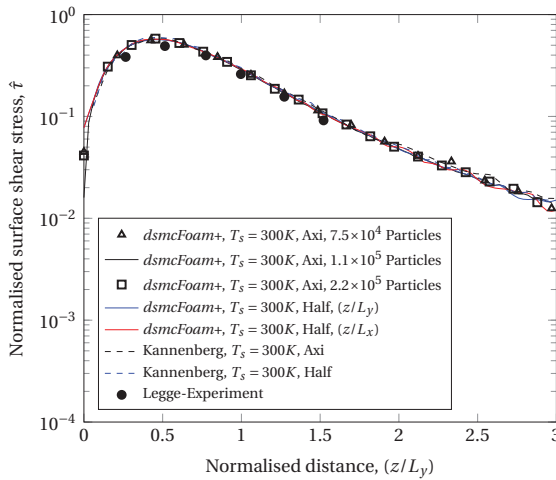
(b) Velocity from the nozzle outlet to the surface.



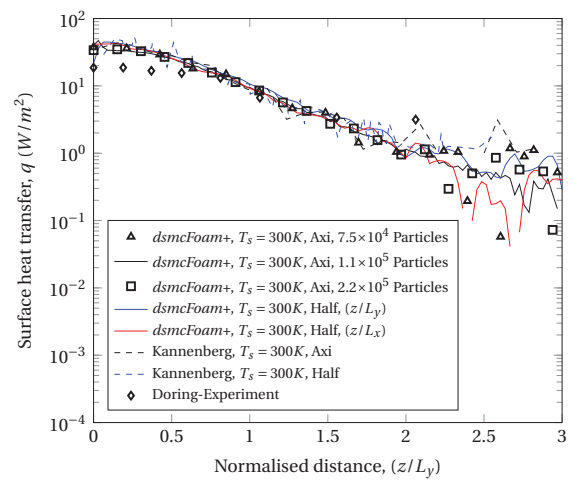
(c) Translational temperature from the nozzle outlet to the surface.



(d) Normalised surface pressure profile.



(e) Normalised surface shear stress profile.



(f) Surface heat transfer profile.

**Fig. 4** Benchmarking of *dsmcFoam+* results against data in the literature. Results are plotted along a radial line starting at the stagnation point.



as a function of the axial distance, i.e.

$$\rho \sim \frac{1}{z^2} [1], \quad (6)$$

when a plume is released in a vacuum environment without any obstruction. However, in this case, the plume impinges on a solid surface, therefore, the density gradually begins to increase again after a normalised distance of 0.7 as the plume is brought to rest by the presence of the solid surface. The plume velocity data shows that the gas initially accelerates as it leaves the sonic nozzle, quickly reaching its limiting velocity,  $u_{lim}$ , which is a function of stagnation temperature, i.e.,

$$u_{lim} = \sqrt{\frac{2\gamma}{\gamma-1} RT_0}. \quad (7)$$

This approach predicts the limit velocity of the gas in the far-field with an assumption that the flow is purely isentropic. As shown in Figure 4(b), the gas velocity reaches the maximum, remains constant for a while, and starts decreasing as it approaches the solid surface. The link between the velocity and temperature distributions can clearly be observed in Figure 4(b). As the gas initially expands, it cools and it then begins to increase in temperature again as it recompressed near the surface. Finally, the temperature very near the surface tends towards the fixed surface temperature of 300 K due to the boundary condition used in the simulations.

## 2. Surface parameters

Figure 4(d) shows the distribution of the surface pressure and, as expected, the total pressure reaches the maximum value at the stagnation point on the surface where the dynamic pressure is very low. As the radial location increases, the dynamic pressure – the stress on the surface can be found using the dynamic pressure for a realistic approach as per Roberts [47, 48]- starts to increase and peaks at

$$\frac{P_{dynmax}}{H} = \sqrt{\frac{2}{(\kappa + 4)}}, \quad (8)$$

where

$$\kappa \equiv \gamma(\gamma - 1)Ma^2 [49]. \quad (9)$$

As observed in Figure 4(e), the surface shear stress is low at the stagnation point and it then increases gradually in proportion to the dynamic pressure. Afterwards, a decreasing trend of both the surface shear stress and the surface pressure is observed.

A simplified heat flux equation of Dettleff [1] for a high angle of attack of the plume impingement is given by

$$\dot{q} \approx \phi \frac{\rho}{2} u^3 \left( 1 - \frac{\gamma + 1}{2\gamma} \frac{T_w}{T_0} \right) \sin \alpha. \quad (10)$$

Herein, the recovery factor, i.e.  $\Lambda \approx 2\gamma/(\gamma + 1)$ , is a non-dimensional parameter of heat transfer at the free molecular impingement indicating when thermal equilibrium, i.e.  $\dot{q} \approx 0$ , is reached during the impingement. If the recovery factor is greater than 1, i.e.  $\Lambda > 1$ , the equilibrium temperature of the plate is greater than the stagnation temperature of the flow [1]. In this case, at the stagnation point, the heat flux in Figure 4(f) shows that there is a relatively small amount of heat transfer observed as the stagnation temperature of the flow is 300 K. However, the translational temperature rises slightly above 300 K as it approaches the surface. Going from the stagnation point on the surface to the far-field, the surface heat transfer quantitatively decreases as seen in Figure 4(f). Dettleff [1] expresses the relation between the heat transfer and distance as

$$\dot{q} \sim \frac{1}{\sqrt{x}}. \quad (11)$$

### 3. Results of *dsmcFoam+* versus others in the literature

Figure 4(a-c) show the distribution of plume parameters from the nozzle outlet to the surface, from two different solvers, *dsmcFoam+* and MONACO [8], for two different mesh topologies; axisymmetric and half-symmetry. Data along the plume impingement axis shows that axisymmetric and half-symmetry simulations of *dsmcFoam+* are complementary and these results also approximately match MONACO's outcomes although there are small deviations between axisymmetric and half-symmetry results.

Considering that there are fewer DSMC simulators per-cell in the half-symmetry simulations, compared to the axisymmetric topology for the same flow field, the statistical fluctuations are larger for *dsmcFoam+* and MONACO solutions as seen in Figures 4(d-f). In addition to the matching data sets of numerical solutions, available experimental measurements are also employed to verify the accuracy of the numerical solutions. Even though the experiments provide a scarce range of data throughout a radial line that starts from the stagnation point to far-field on the surface, both *dsmcFoam+* and MONACO match well, but neither solver recovers the pressure after a normalised distance greater than unity, which suggests that the background pressure in the experiments may have been greater than reported. The heat flux is also over-predicted by both DSMC solvers in comparison to the experiments.

### B. Multi-nozzle normal impingement to the surface at a plume stagnation temperature of 300 K

A motor that has multiple rockets may be employed on spacecraft platforms during maneuvers in a vacuum environment while docking, for rendezvous or maintaining position. Herein, the notable feature is that the resulting plumes impinge on the surface, so the task should be the evaluation of plume-plume interactions, along with plume-surface interactions. Koppenwallner [50] studied the interaction of twin nozzles with different rarefaction levels. In this study, there is an impingement plane between the plumes of two adjacent identical nozzles, named the interaction plane. For free-molecular impingement, it is observed that the plumes simply passed through each other, which is consistent with Ref. [1], where it is stated that an undisturbed mutual plume penetration is possible. To sum up, in order

to understand the changes in a centre of plume core, interaction plane, and the properties of the impingement surface due to the plume-plume impingement as a function of nozzle-to-nozzle distance and increasing stagnation temperature, a simulation matrix is run and the results for plume properties and surface parameters are compared for single, double, and quadruple configurations.

### 1. Plume parameters

As previously emphasised, the local Knudsen number in a plume varies and the flow may become free-molecular before it reaches the impingement surface in this simulated vacuum environment. However, in this case, an assessment is also valuable in deducing the change in the Knudsen number in the region of plume-plume interaction, which allows for the interpretation of how the interaction regime locally alters. The penetration Knudsen number is then defined by

$$Kn_p(\Theta) = \frac{1}{2} \frac{Kn_o}{A_{pl}^o} \frac{D}{2r_n} \frac{1}{\sin^2 \Theta} \frac{1}{f(\Theta)} [1], \quad (12)$$

with

$$A_{pl}^o = A_{pl} \frac{\rho_n}{\rho_o}, \quad (13)$$

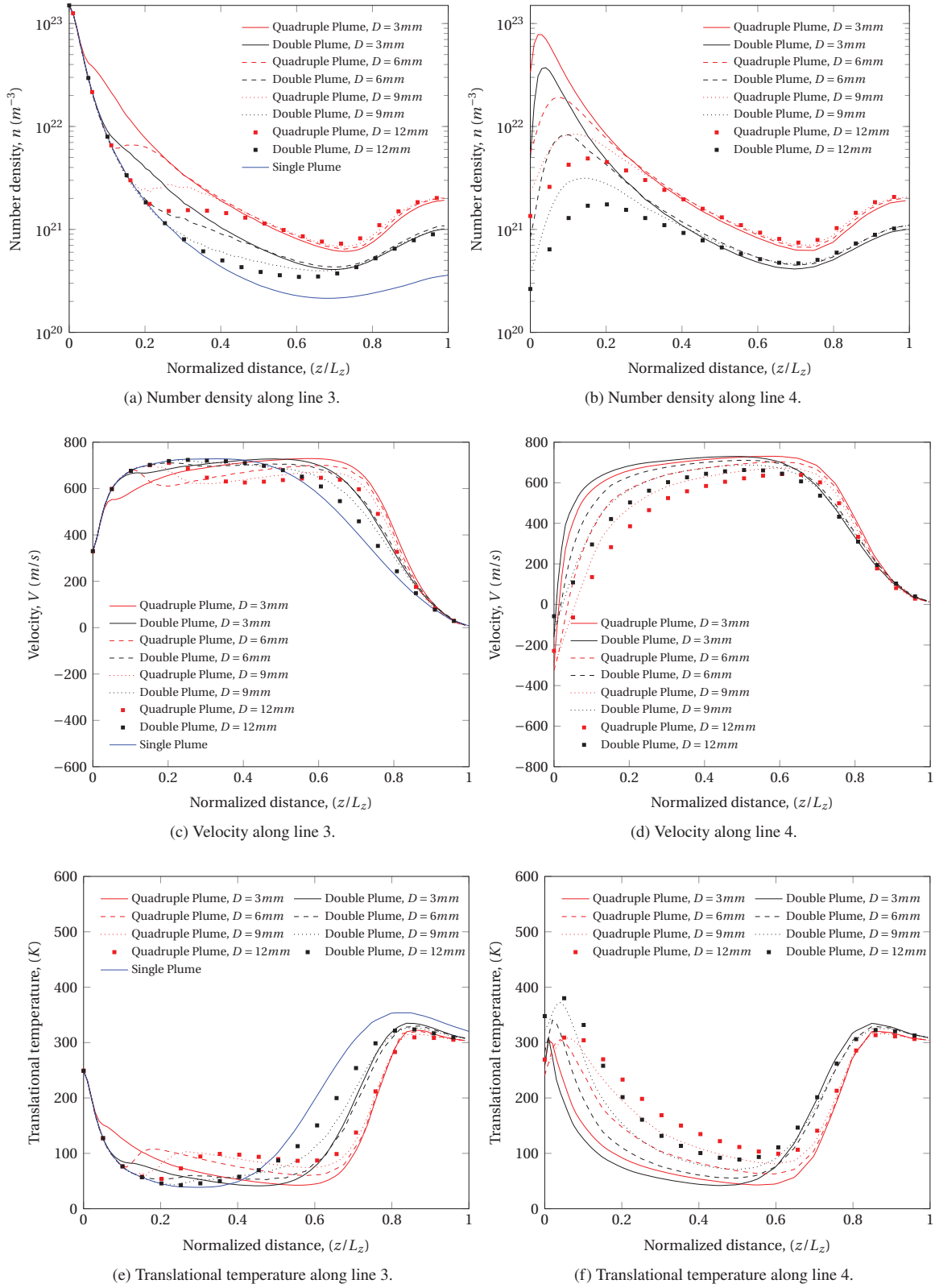
where the distance of  $D/2$ , which is indicated in Figure 2, is the sole parameter that is altered while other variables are kept constant in the impingement simulations of identical nozzles. The local changes in the Knudsen number can also be expressed by the relation of  $\lambda_p \sim 1/\rho_s$ . In addition, the resulting plume impingement on the surface should also be evaluated in order to compare how the aerothermodynamic loading changes through the surface as a function of the number of nozzles and the nozzle-to-nozzle distance in multi-nozzle applications.

In this section, two types of rocket motors, consisting of identical double and quadruple nozzles, hover at a height of  $H = 40$  mm above a solid surface. Furthermore, in order to deduce the effect of the centre-to-centre distance between the nozzles,  $D$  is varied as shown in the simulation matrix of Figure 2. The initial conditions of the flow are maintained as given in Table 1 for  $T_0 = 300$  K.

Figure 5 shows the plume-plume penetration results of *dsmcFoam+* from a nozzle outlet to the surface. The data extraction line is chosen to observe the penetration effect through an axial line, where the lines are:

- *line 3*: from the centre point of one of the nozzle exits to the surface, and
- *line 4*: at the mid-point of the nozzle array, i.e point-C in Figure 3, to the surface.

The distribution of normalised density along line 3 is shown in Figure 5(a) for various separation distances,  $D$ . From the results along line 3, the density distribution is independent of the number of nozzles for a short distance and matches the profile from a single nozzle. As the number of nozzles in the system increases and the distance between the nozzles is held constant, the normalised distance where the profiles diverge moves closer to the origin. The increase in density in the vicinity of the surface is more distinct in the multi-nozzle applications. The mass flow from each nozzle is



**Fig. 5** *dsmcFoam+* results of multi-nozzle plume-plume interactions for changing the distance between the nozzles at  $T_0 = 300$  K.

constant, hence there is a higher mass flow in the multi-nozzle simulations and a higher density near the surface where the plumes have expanded into one another is an expected result. The effect of the distance between the nozzles on the density distribution while the plume is approaching the surface can be compared for the same number of nozzles. In general, as the distance between the nozzles is increased, the normalised location at which the profiles deviate from the single nozzle result increases, with an array of 4 nozzles separated by 3 mm showing the faster deviation as the plumes begin to interact more strongly with one another earlier in the expansion process when they are closer together. In the compression region near the surface, i.e. from a normalised distance of  $\sim 0.7$ , the density profiles become independent of the distance between the nozzles.

Figure 5(b) shows the data extracted along line 4. The density initially increases as the gas expanding from the nozzle exit reaches the centre of the array and then decreases as the gas continues to expand. The effect is more pronounced as the number of nozzles are increased and the spacing between them is decreased. For the same number of nozzles, the profiles become independent of the spacing relatively quickly compared to along line 3; the overall effect of  $D$  becomes negligible after a normalised distance of  $\sim 0.4$ .

Figure 5(c) shows the plume velocity along line 3. As previously discussed in detail, the single plume impingement data from line 3 shows that the plume accelerates after discharging in the vacuum surrounding it and then reaches the limiting velocity, which is reached after a normalised distance of  $\sim 0.2$ . The plume then starts decelerating and stagnates as it arrives at the surface. Examining double plume impingement cases shows the effect of separation distance  $D$  on the plume velocity. For an array of two nozzles with a separation distance of  $D = 12$  mm, the velocity distribution along the impingement axis shows a fairly similar trend with the single-plume, with the deceleration being slightly quicker. Moving the nozzles closer to each other causes a delay in reaching the limiting velocity and allows the gas to move closer to the surface before it begins to decelerate. When an array of four nozzles is considered, the same effects are more pronounced and be observed more clearly.

Figure 5(d) shows the plume velocity along line 4. The velocity is initially negative due the vacuum boundary condition and flow expanding into the region behind the nozzle exit. It should be noted that although the trend of reaching the limiting velocity is in general maintained, it takes a greater normalised distance for this to be reached as the distance between the nozzles increases. The plume from an array of four nozzles decelerates faster than that for an array of two nozzles and the velocity for all cases obtain the same values after a normalised distance of  $\sim 0.9$ , when the flow is being brought to rest by the presence of the solid surface.

Figure 5(e) shows the measurement of translational temperature along line 3. The inverse proportion between the flow velocity and the temperature is clearly explained in Eq. 7. As can be observed from Figures 5(c) and (e), the overall trend of velocity and temperature are in a good agreement, although the translational temperature of the single nozzle does not overlap with the resulting plume of multi-nozzle arrays. As seen in Figures 5(d) and (f), the backflow of the four nozzle array is faster than the double plume configuration, the change in the translational temperature of four nozzle

array is thus slightly lower than in the double nozzle configuration.

## 2. Surface parameters

The aerothermodynamic loading data of the plumes on the surface is extracted along a radial line, named line 5 here, that extends from the stagnation point in a single nozzle array on the surface outwards.

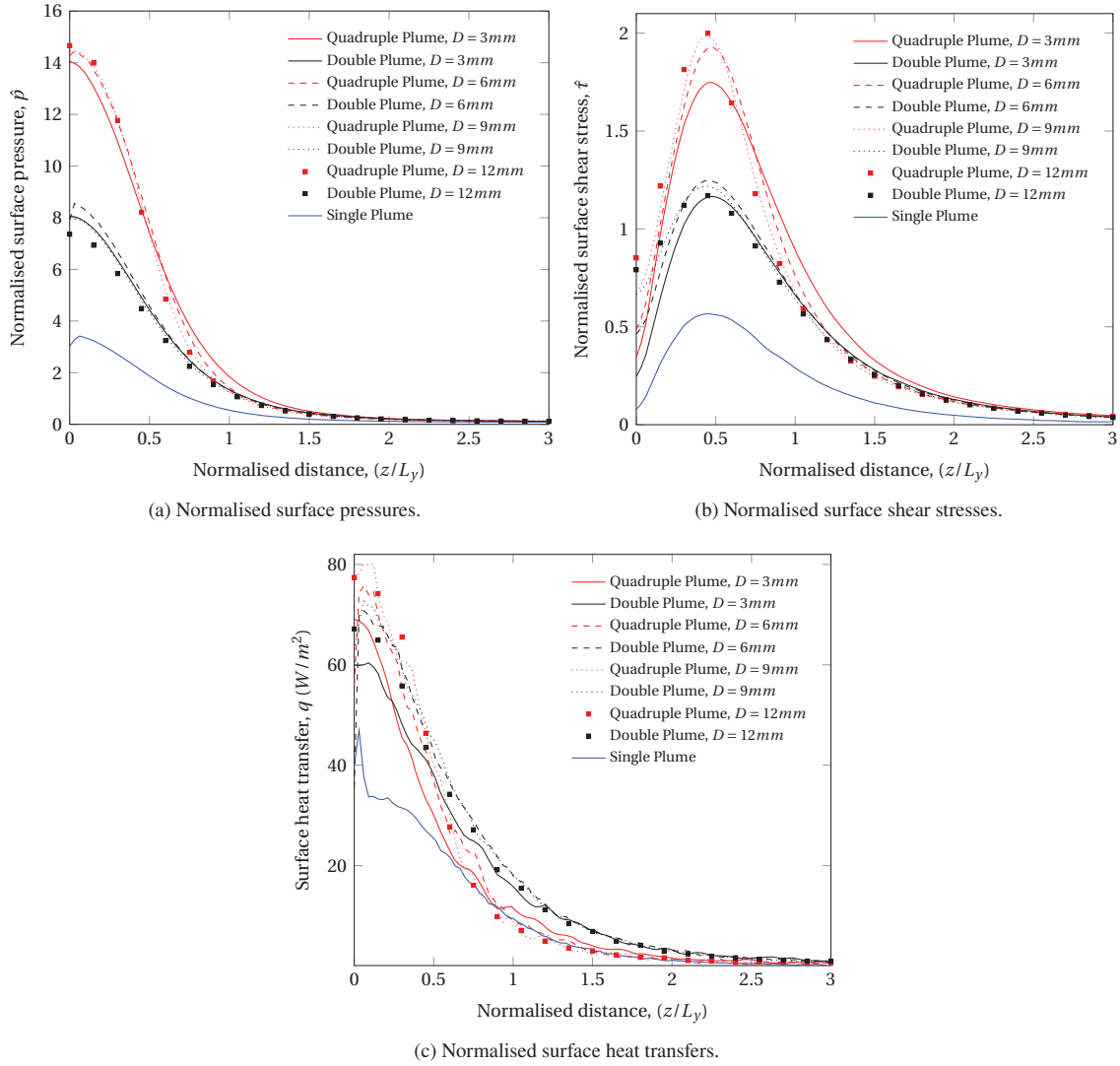
Figure 6 shows the extracted data of plume-surface interactions along line 5. Although the distribution trends of the surface parameters are discussed in detail in Section IV.A.2, the impacts of plume-plume penetration and resulting plumes on the surface show slightly different patterns of surface parameters and quantitatively higher impingement effects than the single plume application. When comparing the surface pressure created by different nozzle arrays at the stagnation point on the surface, it is clear that the surface pressure increases with the number of nozzles, as shown in Figure 6(a). In addition, when comparing the multi-nozzle arrays among themselves, the change in the distance between the nozzles in both double and quadruple arrays does not significantly affect the surface pressure distribution. The differences between the effect of double and quadruple systems disappear in the range of normalised distances between 0.9 and 1.7, where in all cases of four nozzle arrays, the surface pressure decreases gradually, but tighter nozzle arrays introduce a delay in coinciding with the profile for a double nozzle array. Moreover, the surface pressure value becomes equal in single and multi-nozzle systems around the normalised distance of 2.5 on the surface.

Figure 6(b) shows the surface shear profiles. It is observed that the multi-nozzle arrays result in a higher shear stress than the single application at the plume stagnation point on the surface. When a multi-nozzle array within itself is examined, the quadruple simulations at  $D = 3$  mm creates a slightly greater shear stress at the stagnation point than the double one. Following this, with an increasing  $D$ , the results become independent of the number of nozzles in the array; the double and quadruple configurations create the same impact at the stagnation point in terms of shear stress.

The heat transfer rate for multi-nozzle applications is observed to be slightly higher than the single plume impingement around the stagnation point on the surface as shown in Figure 6(c). For each nozzle array configuration, it can be said that the results are almost independent of the nozzle separation distance  $D$  at large radial distance along the surface. Going through the far-field of the surface, the heat transfer rate gradually decreases in inverse proportion with the distance, which is expressed in Eq. 11.

### C. Increasing stagnation temperature in a single nozzle

In order to gain various specific impulse from the motors, the propellants may be fired with different stagnation temperatures. In this work, the stagnation temperature is increased, but the flow remains sonic at the nozzle exit and the stagnation pressure is held constant at 1000 Pa.

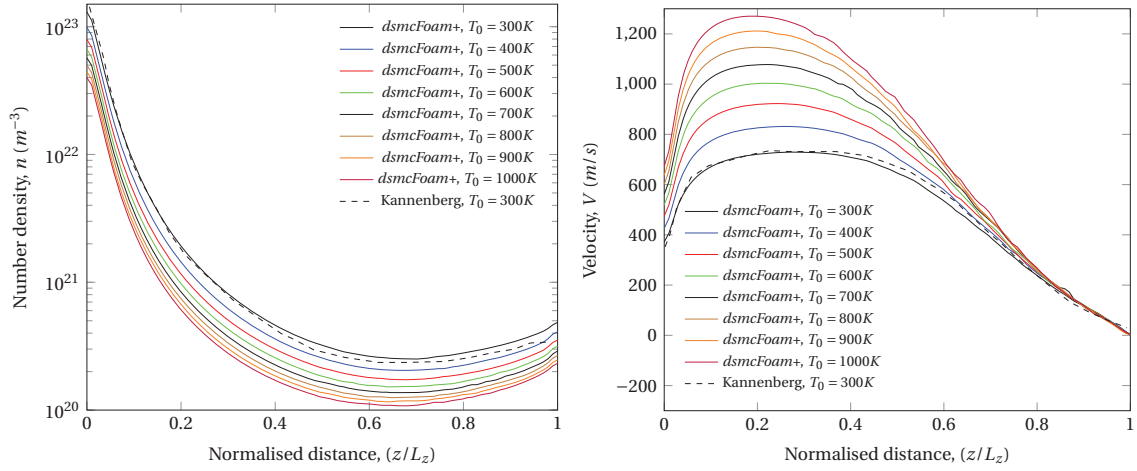


**Fig. 6** *dsmcFoam+* results for surface properties from multi-nozzle arrays at  $T_0 = 300$  K.

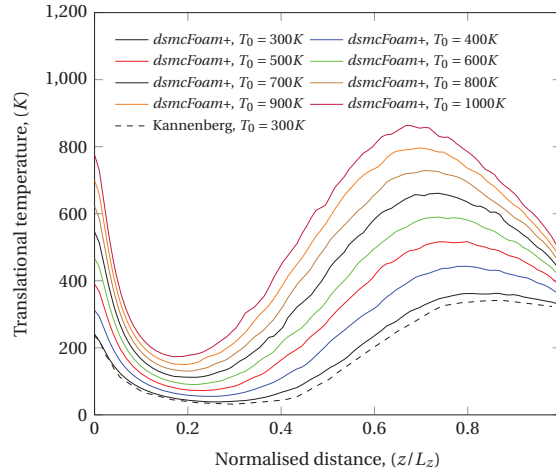
### 1. Plume parameters

In this section, a single nozzle hovers at  $H = 40$  mm above a solid surface and the stagnation temperature of the plume varies from 300 K to 1000 K. Figure 7 shows the properties along an axial data extraction line, which starts from the centre of the nozzle exit and extends to the surface. Figure 7(a) shows the number density along this line. As the stagnation temperature is increased, the inlet number reduces because the stagnation pressure has been held constant at 1000 Pa for all cases. The results for all of the stagnation temperature cases performed here are qualitatively similar, with an initial expansion and recompression near the surface. The density decreases as the stagnation temperature increases.

The velocity profiles throughout the plume centre for different stagnation temperatures is plotted in Figure 7(b). The plume is discharged into the vacuum environment at the sonic velocity,  $V_{sonic} = \sqrt{\gamma RT}$ . Since the stagnation-to-static



(a) Number density from the centre of the nozzle outlet to the surface. (b) Velocity from the centre of the nozzle outlet to the surface.



(c) Translational temperature from the centre of the nozzle outlet to the surface.

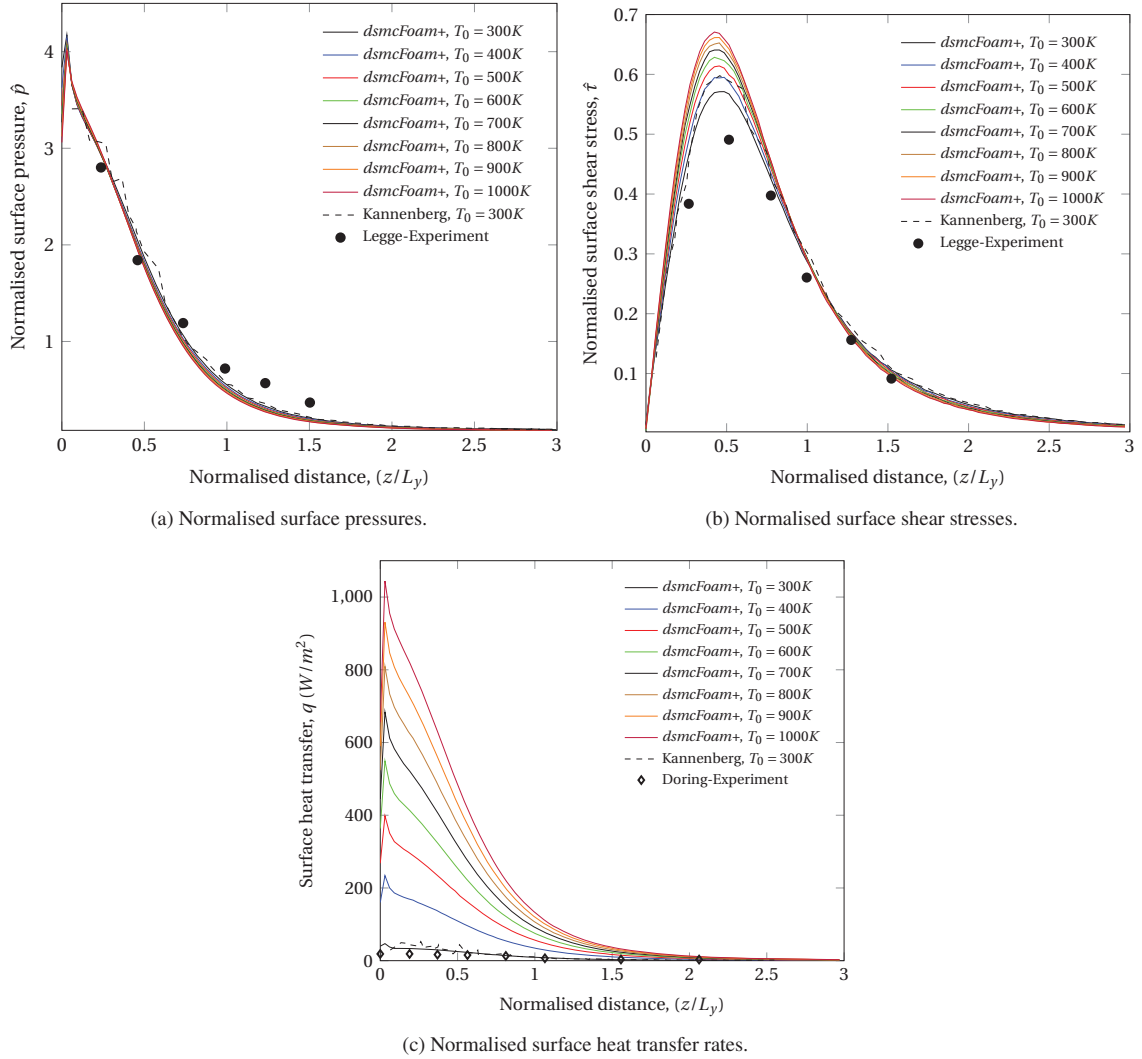
**Fig. 7** *dsmcFoam+* results of single-nozzle plume-surface impingement with increasing stagnation temperature.

temperature ratio remains the same, the inlet velocity increases with the stagnation temperature. It should be also noted that the maximum plume velocity is a function of the stagnation temperature, as given in Eq. 7. In addition, with the increasing stagnation temperature, the distance travelled with the maximum velocity decreases. Figure 7(c) shows the distribution of translational temperature from the nozzle outlet to the impingement surface. The temperatures initially decrease as the gas expands, and then begins to increase as the gas is compressed by the presence of the surface. There is then a further decrease as the gas approaches the surface temperature of 300 K. As the stagnation temperature increases, the gas density decreases, therefore, the degree of rarefaction increases; the result of this is a greater temperature jump as the stagnation temperature increases.



## 2. 2. Surface parameters

At a constant hovering altitude, the peak surface pressure at the impingement point is inversely proportional to the hypersonic parameter as previously explained in Eqs. (8) and (9).



**Fig. 8** *dsmcFoam+* results of single-nozzle plume-surface impingement with increasing stagnation temperature.

The distribution of surface pressure is plotted in Figure 8(a) for the range of stagnation temperatures. At first glance, it is seen that increasing stagnation temperature causes a slight reduction in the surface pressure besides starting at the normalised distance of 0.4. As mentioned previously, a continuous RWF is applied in this study for the axisymmetric domains in order to balance the number of particles from the symmetry axis to further distances according to the change in the volume of DSMC cells. However, this application in axisymmetric solutions causes a measurement error, which is a reduction in the scalar pressure measurement near the surface due to the effect of the number of tentative collisions on

the mean collision time near the axis [44] as can be observed in Figure 8(a) around the stagnation point on the surface.

Figure 8(b) presents the shear stress distribution on the impingement surface for increasing stagnation temperature. It is clearly seen that the shear stress in the vicinity of the stagnation point on the surface is not affected by the changing temperature. Subsequently, the shear stress proportionally increases with the increase in the stagnation temperature up to the normalised distance of 0.5 and shows a decreasing trend until the normalised distance of 1. After this point to the far-field of the surface, the surface shear stress and the stagnation temperature have an inverse proportion as a result of increasing local rarefaction with increasing the stagnation temperature.

For the surface heat transfer, as shown in Figure 8(c), a linear relationship between the stagnation temperature and surface heat transfer can be investigated. It should be also emphasised that a gradual decrease in the proportion between consecutive surface heat transfers as the stagnation temperature increases can be observed. Going through the far-field of the surface, the value of the surface heat transfer gradually decreases at all stagnation temperatures and the surface heating value of all different stagnation temperature cases becomes equal at and after the normalised distance of 2.5.

#### **D. Multi-nozzle normal surface impingement with increasing stagnation temperature**

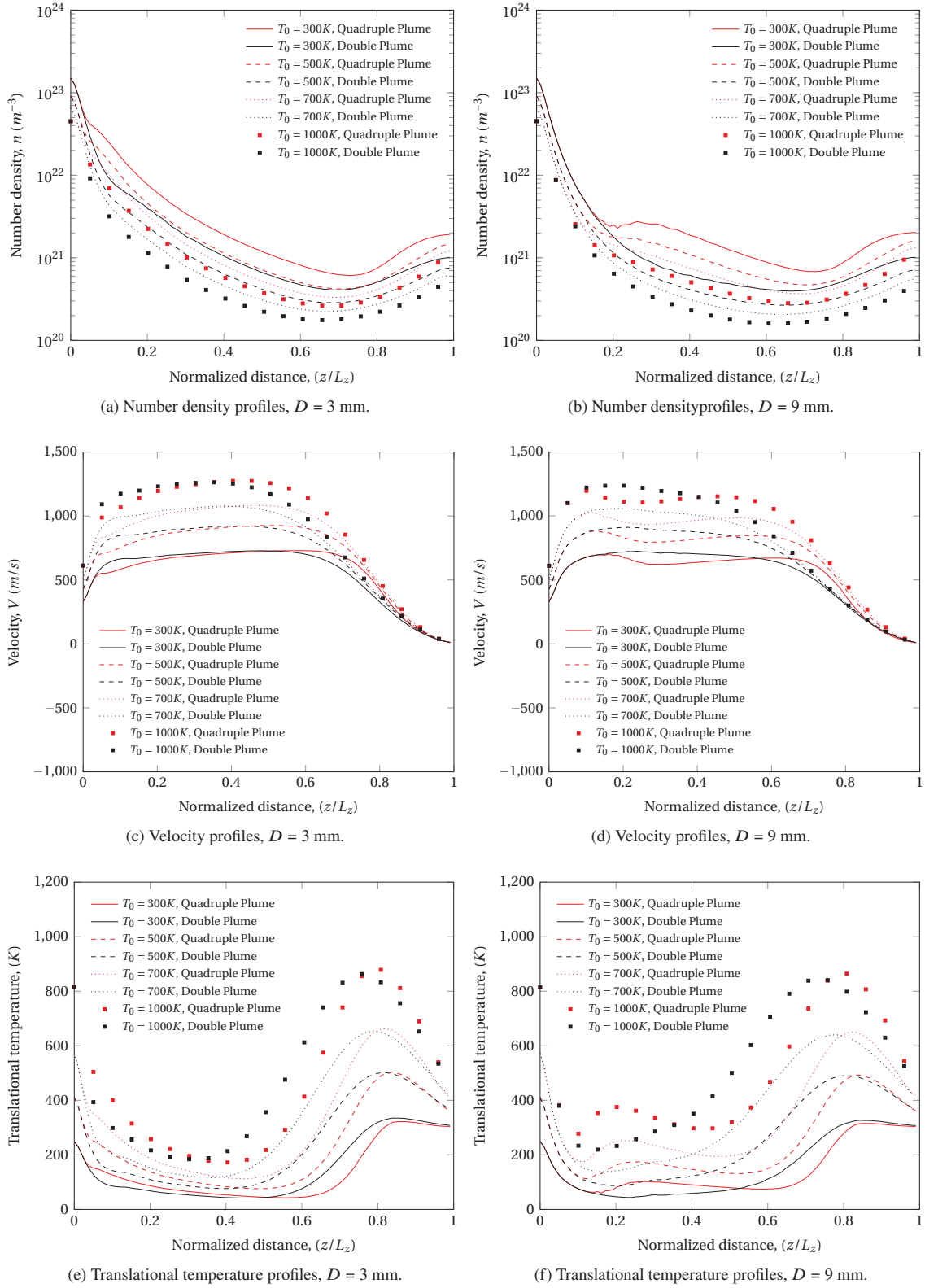
As the increasing stagnation temperature of the plume is discussed for a single nozzle application in the previous section, the multi-nozzle configurations with increasing stagnation temperatures are now considered. In this section, the same flow properties of the single nozzle configuration are applied as inlet parameters for each of the nozzles. While the distance between the motor and the surface is maintained, the stagnation temperature and the nozzle-to-nozzle distances are increased to observe the changes in the resulting plume and the effects of the plume and impingement surface interactions.

##### *1. Plume parameters*

In order to discuss the effect of temperature on the plume-plume interactions, the stagnation temperatures is gradually increased for arrays with two and four nozzles. Furthermore, the impact of nozzle-to-nozzle distance on the plume-plume interaction is also investigated by varying the distance  $D$ .

Figure 9 shows flow profiles for multi-nozzle arrays with increasing stagnation temperatures for the nozzle-to-nozzle distances of  $D = 3$  mm and 9 mm. The data is extracted an axial line, which starts at the centre of a nozzle outlet and extends to the solid surface. Figures 9(a) and (b) show the change in number density along the core of a plume for  $D = 3$  mm and 9 mm, respectively. In general, the profiles for the two different arrays remain similar as the stagnation temperature changes, with the profile being shifted to lower values of density with an increase in temperature. In all cases, the plume initially expands freely, then begins to diverge in shape as two or more plumes begin to interact with one another, but there is still an overall expansion until near the surface where the flow is recompressed.

Figures 9(c) & (d) show the velocity profile of a disrupted plume by the impingement of plume(s) for  $D = 3$  mm



**Fig. 9** *dsmcFoam+* results of multi-nozzle array plume-plume impingement with changing nozzle-to-nozzle distance and increasing stagnation temperature. The results are presented along line 3.

and 9 mm, respectively. The plume-plume interactions disturb the velocity trends of the plume core in some cases, which will be detailed in the following. Herein, the nozzle-to-nozzle distance  $D$ , the number of nozzles in the array, and the stagnation temperature are the key parameters to deduce the location and impact of plume-plume interaction on the velocity profile. Figure 9(c) shows the velocity distributions for multi-nozzle configurations when  $D = 3$  mm. As expected, the penetration effect is more severe in the quadruple array than in the double array, which can be observed with the reduced acceleration of the plume from a normalised distance of 0.05. As the temperature and velocity have a linear relationship, it should also be noted that the velocity profile generated by the quadruple array reaches the same limiting velocity as the double array, but that the deceleration near the surface is delayed for the quadruple arrays. Figure 9(d) presents the data from a plume core while  $D = 9$  mm. The comparison of quadruple and double arrays at all temperatures shows that the disturbance of plume-plume interaction on the velocity profile in the plume core is negligibly small in the double nozzle array compared to the quadruple ones. When compared Figure 9(d) & (e), the location of plume-plume interaction is delayed to around a normalised distance of 0.2 in the quadruple configuration, compared to 0.05 when  $D = 3$  mm. Due to the plume-plume interactions, the gas flow is decelerated and then recovers to its limiting velocity before being decelerated by the presence of the solid surface.

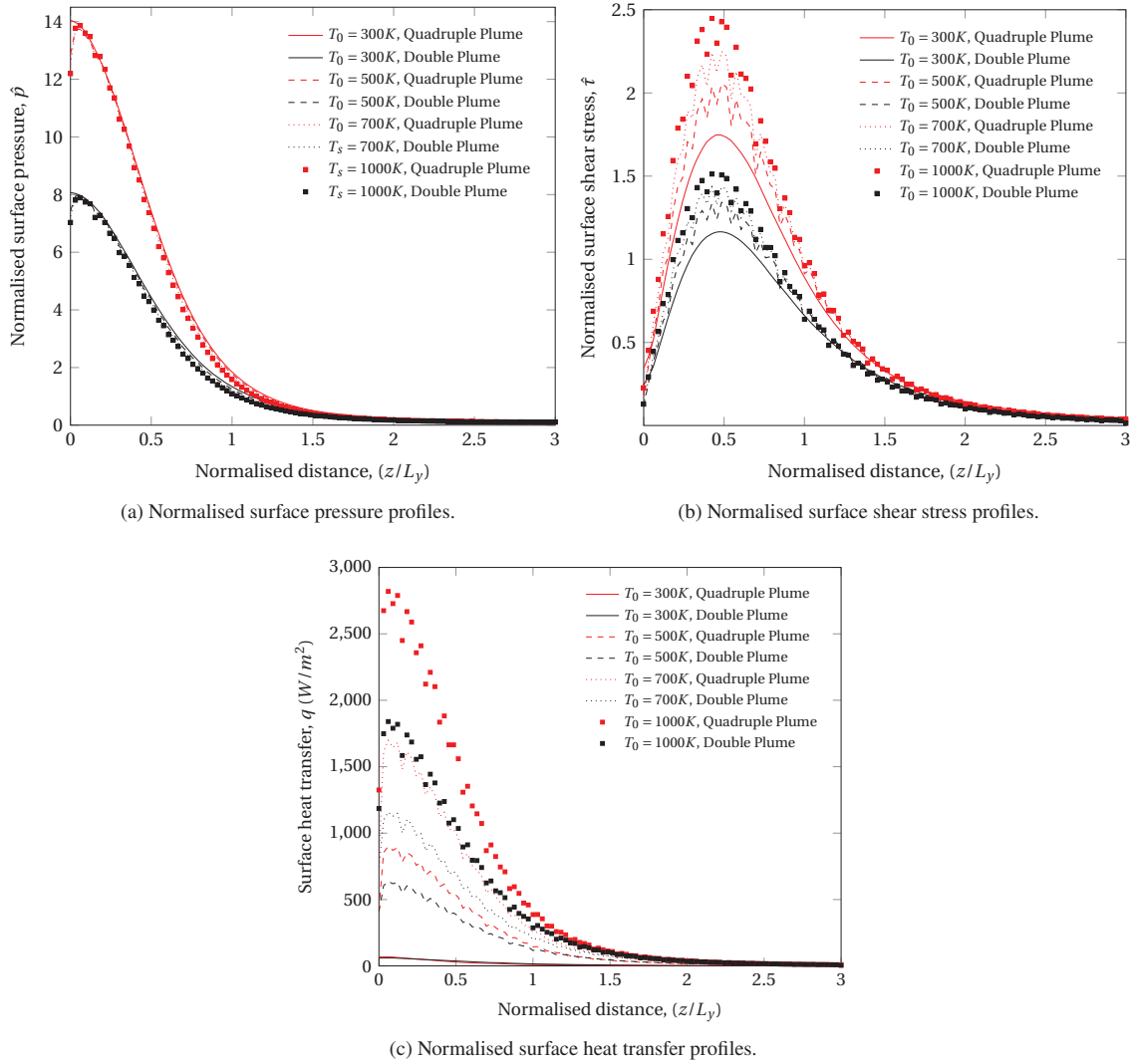
Figures 9(e) & (f) show the temperature profiles in a plume core, including the effect of interaction with other plumes, while the stagnation temperature increases gradually and  $D$  is varied from 3 mm to 9 mm. In all cases, the gas initially cools as it expands, then the temperature begins to increase again as it recompressed near the surface, before finally approaching the constant surface temperature of 300 K. For equal stagnation temperatures, it is clear that the plume temperature decreases less rapidly for a quadruple nozzle array than a double array and that the recompression near the surface is delayed further in a quadruple array. The quadruple and double array profiles remain the same for longer in the  $D = 9$  mm results as it takes longer for the plumes to expand enough to begin interfering with one another. As the stagnation temperature is increased, the temperature profiles are increased all along the normalised distance and there is a larger temperature jump at the surface; this is expected because the larger stagnation temperatures means a lower density in the plume and therefore a higher degree of flow rarefaction.

## 2. Surface parameters

The surface parameters are measured along line 5, as defined in Section IV.B.2. Here, only the surface data for  $D = 3$  mm is shown in Figure 10, as there is negligible difference between the surface impingement data observed at  $D = 3$  mm and various nozzle orientations.

As shown in Figure 6 when the plume temperature is kept constant at 300 K, the distances between the nozzles does not have an impact on the distribution of the surface impingement parameters. However, the number of nozzles in the array quantitatively affects the aerodynamical loading on the surface. It should be highlighted that the surface pressure and surface shear stress are greater in the multi-nozzle arrays rather than the single plume impingement, and that the

quadruple array creates a higher impact at the stagnation point on the surface than the double one. Using the data of the quadruple and double arrays when  $T_0 = 300$  K and  $D = 3$  mm, the results of Figure 6 can be linked to that of Figure 10 in order to enhance the understanding of the effect of the increasing plume stagnation temperature in the multi-nozzle applications on the impingement surface.



**Fig. 10** *dsmcFoam+* results of multi-nozzle plume-surface impingement with increasing stagnation temperature at a constant nozzle-to-nozzle distance,  $D = 3$  mm. The results are plotted along line 5.

Figure 10(a) shows the change in surface pressure as a function of increasing stagnation temperature. The distribution of the surface pressure neither depends on the distance between the nozzles nor the plume temperature. The impingement effect on the surface stagnation point of the quadruple array 1.73 times greater than the double array as discussed previously, regarding the surface impact parameters of resulting plumes in Section IV.B.2.

Figure 10(b), which is the surface shear stress for increasing stagnation temperature at a constant nozzle-to-nozzle

distance of 3 mm, that increasing the stagnation temperature slightly increases the value of the normalised surface shear stress for both double and quadruple arrays.

When the distance between the nozzles is kept constant and the stagnation temperature is gradually increased, the surface heating flux acts as a function of the plume stagnation temperature, as seen in Figure 10(c). The quadruple array causes a higher peak heat transfer to the surface than the double array, however, the difference of the heat transfer value between quadruple and double arrays for the same stagnation temperature disappears around the normalised distance of 1.25.

## V. Conclusion

This work is a study on the effect of changing rocket motor configurations with increasing stagnation temperature on the plume-plume interactions as well as the plume-surface interactions.

The results of constant stagnation temperature with variations in the number and configuration of nozzles show that the increment in number of nozzles and a tighter array results in plume-plume impingement earlier in the axial direction, which results in a quicker deviation from the results of a single plume. Packing the nozzles closer together results in a greater density at the surface stagnation point and delays the recompression near the surface.

When the stagnation temperature is gradually increased in the single plume simulations, the density at the nozzle exit decreases accordingly. The plume with a higher temperature accelerates more quickly. After the recompression, there is a greater temperature jump at the surface as the stagnation temperature increases. For the surface parameters, a denser plume, i.e. one with a lower stagnation temperature, results in a slightly greater impact on the surface in terms of normalised pressure, but the opposite trend is observed for the normalised shear stress and the surface heat transfer, with the higher stagnation temperatures resulting in greater impacts on the surface properties.

In another application, the number of nozzles and the stagnation temperature are increased, while the distance between the nozzles is altered. The examination of the resulting plume-plume impingement indicates that the colder and more tightly packed arrays with more nozzles result in an earlier and a greater impact on the density trend along an axial line from a nozzle exit. Increasing the stagnation temperature accelerates the gas to a higher velocity, but the resulting plumes, independent of the number of nozzles, decelerate far downstream of the nozzle exit and stagnate on the surface. The trend of the translational temperature changes in the plume core region along the impingement axis as a result of plume-plume penetration. However, quadruple and double nozzle arrays at the same stagnation temperatures reach the surface with the same temperatures and the effect of the distance between the nozzles become negligible. This is also applicable for the surface parameters as the impingement effect is not a function of the nozzle-to-nozzle distance. Quadruple arrays result a higher surface pressure at the stagnation point than double arrays, but the surface pressure becomes equal for all cases at a large radial distance. For the normalised surface pressure data, the number of nozzles is more significant than the stagnation temperature. However, a slight effect of the stagnation temperature can be found on

the normalised surface shear stress. A flow with a higher stagnation temperature and more nozzles produces a slightly higher normalised surface shear stress. As expected, greater stagnation temperatures result a higher heat flux on the surface, but also in the vicinity of the impingement region while the effect of the number of nozzle is clearly observed. The effect of the number of nozzles at higher plume temperatures disappear at a large radial distance.

The results in this work have been limited to sonic nozzles. Future work should consider supersonic flow at the nozzle exits.

### Funding Sources

M. B. Agir's research is sponsored by the Republic of Turkey's Ministry of National Education (MoNE-1416/YLSY).

### Acknowledgments

The authors thank the University of Glasgow's computational cluster facilities, including Buckethead and Headnode high performance computers.

### References

- [1] Dettleff, G., "Plume Flow and Plume Impingement in Space Technology," *Progress in Aerospace Sciences*, Vol. 28, No. 1, 1991, pp. 1–71. [https://doi.org/10.1016/0376-0421\(91\)90008-R](https://doi.org/10.1016/0376-0421(91)90008-R).
- [2] Vick, A. R., "Rocket Exhaust-plume Problems and Some Recent Related Research," *The Fluid Dynamic Aspects of Space Flight*, 1966, pp. 129–180.
- [3] Boettcher, R., and Legge, H., *A Study of Rocket Exhaust Plumes and Impingement Effects on Spacecraft Surfaces–I. Literature Survey*, Publication IB 251-80 A 27, DFVLR Internal Report, Göttingen, 1980.
- [4] Lengrad, J. C., "Plume Impingement upon Spacecraft Surfaces," *Proceedings of the 14th International Symposium on Rarefied Gas Dynamics*, University of Tokyo Press, Tokyo, 1984, pp. 217–228.
- [5] Boyd, I. D., Jafry, Y., and Beukel, J. V., "Particle Simulations of Helium Microthruster Flows," *Journal of Spacecraft and Rockets*, Vol. 31, No. 2, 1994, pp. 271–277. <https://doi.org/10.2514/3.26433>.
- [6] Piesik, E., Koppang, R., and Simkin, D., "Rocket-exhaust Impingement on a Flat Plate at High Vacuum," *Journal of Spacecraft and Rockets*, Vol. 3, No. 11, 1966, pp. 1650–1657. <https://doi.org/10.2514/3.28720>.
- [7] Deependran, B., Sujith, R., and Kurian, J., "Studies of Low-density Freejets and Their Impingement Effects," *AIAA journal*, Vol. 35, No. 9, 1997, pp. 1536–1542. <https://doi.org/10.2514/2.7482>.
- [8] Kannenberg, K. C., *Computational Methods for the direct simulation Monte Carlo Technique with Application to Plume Impingement*, Doctoral Dissertation. Cornell University, NY, 1998.

- [9] Legge, H., “Plume Impingement Forces on Inclined Flat Plates,” *Rarefied Gas Dynamics*, 1991, pp. 955–962.
- [10] Döring, S., *Experimental Plume Impingement Heat Transfer on Inclined Flat Plates*, Publication 222-90 A 36, DLR Internal Report, Göttingen, 1990.
- [11] Mehta, M., “Rocket Plume Interactions for NASA Landing Systems,” <https://ntrs.nasa.gov/citations/20200000979>, 2019. Accessed Aug. 21, 2021.
- [12] Ivanov, M., Markelov, G., Gerasimov, Y. I., Krylov, A., Mishina, L., and Sokolov, E., “Free-flight Experiment and Numerical Simulation for Cold Thruster Plume,” *Journal of Propulsion and Power*, Vol. 15, No. 3, 1999, pp. 417–423. <https://doi.org/10.2514/2.5460>.
- [13] Ivanov, S., Markelov, N., Kashkovsky, V., and Giordano, D., “Numerical Analysis of Thruster Plume Interaction Problems,” *European Spacecraft Propulsion Conference*, Vol. 398, 1997, p. 603.
- [14] Lumpkin, F., III, Stuart, P., and Le Beau, G., “Enhanced Analyses of Plume Impingement During Shuttle-Mir Docking Using a Combined CFD and DSMC Methodology,” *31st Thermophysics Conference*, 1996, p. 1877. <https://doi.org/10.2514/6.1996-1877>.
- [15] Lee, K. H., Lee, S. N., Yu, M. J., Kim, S. K., and Baek, S. W., “Combined Analysis of Thruster Plume Behavior in Rarefied Region by Preconditioned Navier-Stokes and DSMC Methods,” *Transactions of the Japan Society for Aeronautical and Space Sciences*, Vol. 52, No. 177, 2009, pp. 135–143. <https://doi.org/https://doi.org/10.2322/tjsass.52.135>.
- [16] George, J. D., *A Combined CFD-DSMC Method for Numerical Simulation of Nozzle Plume Flows*, Doctoral Dissertation. Cornell University, NY, 2000.
- [17] Boyd, I., and Stark, J., “Modeling of a Small Hydrazine Thruster Plume in the Transition Flow Regime,” *Journal of Propulsion and Power*, Vol. 6, No. 2, 1990, pp. 121–126. <https://doi.org/10.2514/3.23232>.
- [18] Legge, H., and Boettcher, R.-D., “Modelling Control Thruster Plume Flow and Impingement,” *Rarefied Gas Dynamics*, Springer, 1985, pp. 983–992. [https://doi.org/10.1007/978-1-4613-2467-6\\_31](https://doi.org/10.1007/978-1-4613-2467-6_31).
- [19] Hoffman, R., Kawasaki, A., Trinks, H., Bindemann, I., and Ewering, W., “The CONTAM 3.2 Plume Flowfield Analysis and Contamination Prediction Computer Program-Analysis Model and Experimental Verification,” *20th Thermophysics Conference*, 1985, p. 928. <https://doi.org/10.2514/6.1985-928>.
- [20] Boyd, I., and Stark, J., “Assessment of Impingement Effects in the Isentropic Core of a Small Satellite Control Thruster Plume,” *Proceedings of the Institution of Mechanical Engineers, Part G: Journal of Aerospace Engineering*, Vol. 203, No. 2, 1989, pp. 97–103. [https://doi.org/10.1243/PIME\\_PROC\\_1989\\_203\\_060\\_01](https://doi.org/10.1243/PIME_PROC_1989_203_060_01).
- [21] Mahdavi, A., and Roohi, E., “A novel hybrid DSMC-Fokker Planck algorithm implemented to rarefied gas flows,” *Vacuum*, Vol. 181, 2020, p. 109736. <https://doi.org/10.1016/j.vacuum.2020.109736>.
- [22] Darbandi, M., and Roohi, E., “Study of subsonic–supersonic gas flow through micro/nanoscale nozzles using unstructured DSMC solver,” *Microfluidics and Nanofluidics*, Vol. 10, No. 2, 2011, pp. 321–335. <https://doi.org/10.1007/s10404-010-0671-7>.



- [23] Saadati, S. A., and Roohi, E., “Detailed investigation of flow and thermal field in micro/nano nozzles using Simplified Bernoulli Trial (SBT) collision scheme in DSMC,” *Aerospace Science and Technology*, Vol. 46, 2015, pp. 236–255. <https://doi.org/10.1016/j.ast.2015.07.013>.
- [24] Mehta, M., Canabal, F., Tashakkor, S. B., and Smith, S. D., “Numerical Base Heating Sensitivity Study for a Four-rocket Engine Core Configuration,” *Journal of Spacecraft and Rockets*, Vol. 50, No. 3, 2013, pp. 509–526. <https://doi.org/10.2514/1.A32287>.
- [25] Rault, D., “Methodology for Thruster Plume Simulation and Impingement Effects Characterization Using DSMC,” *30th Thermophysics Conference*, 1995, p. 2032. <https://doi.org/10.2514/6.1995-2032>.
- [26] Boyd, I. D., Penko, P. F., Meissner, D. L., and DeWitt, K. J., “Experimental and Numerical Investigations of Low-density Nozzle and Plume Flows of Nitrogen,” *AIAA Journal*, Vol. 30, No. 10, 1992, pp. 2453–2461. <https://doi.org/10.2514/3.11247>.
- [27] Garcia, A. L., *Numerical Methods for Physics*, Prentice Hall Englewood Cliffs, NJ, 2000.
- [28] Bird, G., “Breakdown of Translational and Rotational Equilibrium in Gaseous Expansions,” *AIAA Journal*, Vol. 8, No. 11, 1970, pp. 1998–2003. <https://doi.org/10.2514/3.6037>.
- [29] Bird, G., *Molecular Gas Dynamics and the direct simulation Monte Carlo of Gas Flows*, Clarendon, Oxford, 1994.
- [30] White, C., *Benchmarking, Development and Applications of an Open Source DSMC Solver*, Doctoral Dissertation. University of Strathclyde, Glasgow, UK, 2013.
- [31] Prasanth, P., and Kakkassery, J. K., “Direct simulation Monte Carlo (DSMC): A Numerical Method for Transition-regime Flows-A review,” *Journal of the Indian Institute of Science*, Vol. 86, No. 3, 2013, p. 169.
- [32] Bird, G., *The DSMC Method*, CreateSpace Independent Publishing Platform, 2013.
- [33] Hadjiconstantinou, N. G., Garcia, A. L., Bazant, M. Z., and He, G., “Statistical Error in Particle Simulations of Hydrodynamic Phenomena,” *Journal of Computational Physics*, Vol. 187, No. 1, 2003, pp. 274–297. [https://doi.org/10.1016/S0021-9991\(03\)00099-8](https://doi.org/10.1016/S0021-9991(03)00099-8).
- [34] Stefanov, S. K., “On DSMC Calculations of Rarefied Gas Flows with Small Number of Particles in Cells,” *SIAM Journal on Scientific Computing*, Vol. 33, No. 2, 2011, pp. 677–702. <https://doi.org/10.1137/090751864>.
- [35] Venkatraman, A., Alexeenko, A. A., Gallis, M., and Ivanov, M., “A Comparative Study of No-time-counter and Majorant Collision Frequency Numerical Schemes in DSMC,” *AIP Conference Proceedings*, Vol. 1501, American Institute of Physics, 2012, pp. 489–495. <https://doi.org/10.1063/1.4769577>.
- [36] Taheri, E., Roohi, E., and Stefanov, S., “A symmetrized and simplified Bernoulli trial collision scheme in direct simulation Monte Carlo,” *Physics of Fluids*, Vol. 34, No. 1, 2022, p. 012010. <https://doi.org/10.1063/5.0076025>.
- [37] Roohi, E., Stefanov, S., Shoja-Sani, A., and Ejraei, H., “A generalized form of the Bernoulli Trial collision scheme in DSMC: Derivation and evaluation,” *Journal of Computational Physics*, Vol. 354, 2018, pp. 476–492. <https://doi.org/10.1016/j.jcp.2017.10.033>.

- [38] Goshayeshi, B., Roohi, E., and Stefanov, S., “DSMC simulation of hypersonic flows using an improved SBT-TAS technique,” *Journal of Computational Physics*, Vol. 303, 2015, pp. 28–44. <https://doi.org/10.1016/j.jcp.2015.09.027>.
- [39] Amiri-Jaghargh, A., Roohi, E., Niazmand, H., and Stefanov, S., “DSMC Simulation of Low Knudsen Micro/Nanoflows Using Small Number of Particles per Cells,” *Journal of Heat Transfer*, Vol. 135, No. 10, 2013. <https://doi.org/10.1115/1.4024505>.
- [40] Bird, G., “Definition of Mean Free Path for Real Gases,” *The Physics of Fluids*, Vol. 26, No. 11, 1983, pp. 3222–3223. <https://doi.org/10.1063/1.864095>.
- [41] Scanlon, T., Roohi, E., White, C., Darbandi, M., and Reese, J., “An Open Source, Parallel DSMC Code for Rarefied Gas Flows in Arbitrary Geometries,” *Computers & Fluids*, Vol. 39, No. 10, 2010, pp. 2078–2089. <https://doi.org/10.1016/j.compfluid.2010.07.014>.
- [42] White, C., Borg, M. K., Scanlon, T. J., and Reese, J. M., “A DSMC Investigation of Gas Flows in Micro-channels with Bends,” *Computers & Fluids*, Vol. 71, 2013, pp. 261–271. <https://doi.org/10.1016/j.compfluid.2012.10.023>.
- [43] White, C., Borg, M. K., Scanlon, T. J., Longshaw, S. M., John, B., Emerson, D., and Reese, J. M., “dsmcFoam+: An OpenFOAM Based direct simulation Monte Carlo Solver,” *Computer Physics Communications*, Vol. 224, 2018, pp. 22–43. <https://doi.org/10.1016/j.cpc.2017.09.030>.
- [44] Liechty, D. S., “Modifications to Axially Symmetric Simulations Using New DSMC (2007) Algorithms,” *AIP Conference Proceedings*, Vol. 1084, American Institute of Physics, 2008, pp. 251–256. <https://doi.org/10.1063/1.3076481>.
- [45] Chambre, P. A., and Schaaf, S. A., *Flow of Rarefied Gases*, Princeton University Press, 2017. <https://doi.org/10.1515/9781400885800>.
- [46] Simons, G. A., “Effect of Nozzle Boundary Layers on Rocket Exhaust Plumes,” *AIAA Journal*, Vol. 10, No. 11, 1972, pp. 1534–1535. <https://doi.org/10.2514/3.6656>.
- [47] Roberts, L., “The Action of a Hypersonic Jet on a Dusty Surface,” *Proceedings of 31st Annual Meeting of the Institute of Aerospace Science*, 1963, pp. 63–50.
- [48] Roberts, L., “The Interaction of a Rocket Exhaust with the Lunar Surface (Rocket Exhaust Jet Interaction with Lunar Surface Dust Layer),” *Agard the Fluid Dyn. Aspects of Space Flight*, Vol. 2, 1966.
- [49] Morris, A. B., *Simulation of Rocket Plume Impingement and Dust Dispersal on the Lunar Surface*, Doctoral Dissertation. The University of Texas at Austin, 2012.
- [50] Koppenwallner, G., “Scaling Laws for Rarefied Plume Interference with Application to Satellite Thrusters,” *International Symposium on Space Technology and Science, 14th, Tokyo, Japan*, 1984, pp. 505–512.